Scattering of individual particles from cytometry: tests on phytoplankton cultures

William Moutier, Lucile Duforêt-Gaurier, Melilotus Thyssen, Hubert Loisel, Xavier Mériaux, Lucie Courcot, David Dessailly, Séverine Alvain

Research Article | Vol. 24, No. 21 | 17 Oct 2016 | OPTICS EXPRESS 24188

Optics EXPRESS

Scattering of individual particles from cytometry: tests on phytoplankton cultures

W. MOUTIER,[1,*] L. DUFORÊT-GAURIER,[1] M. THYSSEN,[2] H. LOISEL,[1,3,4] X. MÉRIAUX,[1] L. COURCOT,[1] D. DESSAILLY,[1] AND S. ALVAIN[1]

[1]*Laboratoire d'Océanologie et de Géosciences (LOG), Université du Littoral Cote d'Opale (ULCO), CNRS UMR 8187, 32 avenue Foch, 62930 Wimereux, France*
[2]*Mediterranean Institute of Oceanography (MIO), Université d'Aix-Marseille (AMU), CNRS/IRD UMR 7294, Campus de Luminy, 13288 Marseille, France*
[3]*Institut de Recherche pour le Développement (IRD), Université de Toulouse, UPS (OMP), CNRS, UMR 5566 LEGOS, 14 avenue Edouard Belin, 31400 Toulouse, France*
[4]*Space Technology Institute (STI), Vietnam Academy of Science and Technology (VAST), 18 Hoang Quoc Viet, Cau Giay, Hanoi, Vietnam*
william.moutier@univ-littoral.fr

Abstract: This study presents an application of the Cytosense flow cytometer (CytoBuoy b.v., NL) for the analysis of the optical properties of phytoplankton cells. For the first time, the forward, sideward and backward cross sections (σ_{FSC}, σ_{SSC} and σ_{b_b}) were derived for two species morphologically different (*Chlamydomonas concordia* and *Thalassiosira pseudonana*). The objective of this work is to check the validity of the estimates before any applications in the frame of marine optics studies. Thus, estimates of σ_{FSC} and σ_{SSC} are tested with radiative transfer computations as no in situ measurements are available. A synthetic database is built considering homogeneous, multi-layered spheres, aggregates and cylinders. Scanning electron micrographs were performed to investigate the cell morphology to simulate particles as close as possible to the real cells. This set of numerical results represents a valuable database for many kinds of applications dealing with marine optics. Comparisons showed that the Cytosense estimates for the cultures are consistent with values predicted by the theory. In average, more than 92% of the Cytosense estimates were encompassed by predicted values. The backscattering cross section and the backscattering efficiency were compared with in situ measurements found in the literature wherever possible. Results showed that σ_{b_b} and Q_{b_b} estimations fall within the range of the referenced values.

OCIS codes: (010.4450) Oceanic optics; (010.5620) Radiative transfer; (010.1350) Backscattering; (120.4640) Optical instruments; (120.5820) Scattering measurements; (290.5850) Scattering, particles.

References and links

1. R. W. Preisendorfer, "Secchi disk science: Visual optics of natural waters," Limnol. Oceanogr. **31**(5), 909–926 (1986).
2. A. Bricaud, J. R. V. Zaneveld, and J. C. Kitchen, "Backscattering efficiency of coccolithophorids: use of a three-layered sphere model," Proc. SPIE. **1750**, 27–33 (1992).
3. J. C. Kitchen, and J.R. V. Zaneveld, "A three-layered sphere model of the optical properties of phytoplankton," Limnol. Oceanogr. **37**(8), 1680–1690 (1992).
4. R. A. Meyer and A. Brunsting, "Light scattering from nucleated biological cells," Biophysical journal. **15**, 191–203 (1975).
5. R. A. Meyer, "Light scattering from biological cells: dependence of backscatter radiation on membrane thickness and refractive index," Appl. Opt. **18**(5), 585–588 (1979).
6. A. Quirantes and S. Bernard, "Light scattering by marine algae: two-layer spherical and nonspherical models," J. Quant. Spectrosc. Radiat. Transf. **89**, 311–321 (2004).
7. J. R. V. Zaneveld and J. C. Kitchen, "The variation in the inherent optical properties of phytoplankton near an absorption peak as determined by various models of cell structure," J. Geophys. Res. **100**(C7), 309–313 (1995).
8. S. Bernard, T. A. Probyn and A. Quirantes, "Simulating the optical properties of phytoplankton cells using a two-layered spherical geometry," Biogeosci. Discuss. **6**, 1497–1563 (2009).

#266681 http://dx.doi.org/10.1364/OE.24.024188
Journal © 2016 Received 20 May 2016; revised 8 Jul 2016; accepted 15 Jul 2016; published 11 Oct 2016

Optics EXPRESS

9. G. Dall'Olmo, E. Boss, M. J. Behrenfeld, and T. K. Westberry, "Particulate optical scattering coefficients along an Atlantic Meridional Transect," Opt. Express. **20**(19), 21532–21551 (2012).
10. M. W. Matthews and S. Bernard, "Using a two-layered sphere model to investigate the impact of gas vacuoles on the inherent optical properties of M. aeruginosa," Biogeosci. Discuss. **10**(6), 10531–10579 (2013).
11. M. S. Quinby-Hunt and A. J. Hunt, "Polarized-light scattering studies of marine Chlorella," Limnol. Oceanogr. **34**(8), 1587–1600 (1989).
12. A. Quirantes and S. Bernard, "Light-scattering methods for modelling algal particles as a collection of coated and/or nonspherical scatterers," J. Quant. Spectrosc. Radiat. Transf. **100**, 315–324 (2006).
13. O. Svensen, O. Frette, and S. R. Erga, "Scattering properties of microalgae: the effect of cell size and cell wall," Appl. Opt. **46**(23), 5762–5769 (2007).
14. D. Stramski and C. D. Mobley, "Effects of microbial particles on oceanic optics: A database of single-particle optical properties," Limnol. Oceanogr. **42**(3), 538–549 (1997).
15. D. Stramski, A. Bricaud, and A. Morel, "Modeling the inherent optical properties of the ocean based on the detailed composition of the planktonic community," Appl. Opt. **40**(18), 2929–2945 (2001).
16. Y.-H. Ahn, A. Bricaud, and A. Morel, "Light backscattering efficiency and related properties of some phytoplankters," Deep-Sea Res. **39**(11/12), 1835–1855 (1992).
17. D. Stramski, and D. A. Kiefer, "Light scattering by microorganisms in the open ocean," Prog. Oceanogr. **28**, 343–383 (1991).
18. A. Morel, and A. Bricaud, "Inherent optical properties of algal cells including picoplankton: Theoretical and experimental results," Can. Bull. Fish. Aquat. Sci. **214**, 521–559 (1986).
19. A. Bricaud, A. Morel, and L. Prieur, "Optical Efficiency Factors of Some Phytoplankters," Limnol. Oceanogr. **28**(5), 816–832 (1983).
20. A. Bricaud, and A. Morel, "Light attenuation and scattering by phytoplanktonic cells: a theoretical modeling," Appl. Opt. **25**(4), 571–580 (1986).
21. A. Morel, and Y-H. Ahn, "Optics of heterotrophic nanoflagellates and ciliates: A tentative assessment of their scattering role in oceanic waters compared to those of bacterial and algal cells," J. Mar. Res. **49**, 177âĂŞ202 (1991).
22. H. Volten, J. F. D. Haan, and J. W. Hovenier, "Laboratory measurements of angular distributions of light scattered by phytoplankton and silt," Limnol. Oceanogr. **43**(6), 1180–1197 (1998).
23. G. B. J. Dubelaar, J. W. Visser, and M. Donze, "Anomalous behaviour of forward and perpendicular light scattering of a cyanobacterium owing to intracellular gas vacuoles," Cytometry. **8**(4), 405–412 (1987).
24. K. J. Voss, "Scattering and attenuation properties of Emiliania huxleyi cells and their detached coccoliths," Limnol. Oceanogr. **43**(5), 870–876 (1998).
25. K. Witkowski, T. Król, A. Zielinski, and E. Kuten, "A light-scattering matrix for unicellular marine phytoplankton," Limnol. Oceanogr. **43**(5), 859–869 (1998).
26. K. Witkowski, L. Woliriski, and Z. Turzyliski, "The investigation of kinetic growth of Chlorella vulgaris cells by the method of integral and dynamic light scattering," Limnol. Oceanogr. **38**(7), 1365–1372 (1993).
27. R. D. Vaillancourt, C. W. Brown, R. R. L. Guillard, and W. M. Balch, "Light backscattering properties of marine phytoplankton: relationships to cell size, chemical composition and taxonomy," J. Plankton Res. **26**(2), 191–212 (2004).
28. A. L. Whitmire, W. S. Pegau, and L. Karp-Boss, "Spectral backscattering properties of marine phytoplankton cultures," Opt. Express. **18**(14), 1680–1690 (2010).
29. R. E. Green, H. M. Sosik, R. J. Olson, and M. D. DuRand, "Flow cytometric determination of size and complex refractive index for marine particles: comparison with independent and bulk estimates," Appl. Opt. **42**(3), 526–541 (2003).
30. R. E. Green, H. M. Sosik, and R. J. Olson, "Contributions of phytoplankton and other particles to inherent optical properties in New England continental shelf waters," Limnol. Oceanogr. **48**(6), 2377–2391 (2003).
31. L. Duforêt-Gaurier, W. Moutier, N. Guiselin, M. Thyssen, G. B. J. Dubelaar, X. Mériaux, L. Courcot, D. Dessailly, and H. Loisel, "Determination of backscattering cross section of individual particles from cytometric measurements: a new methodology," Opt. Express. **23**(24), 31510–31533 (2015).
32. M. I. Mishchenko, "Calculation of the amplitude matrix for a nonspherical particle in a fixed orientation," Appl. Opt. **39**(6), 1026–1031 (2000).
33. Y. L. Xu, and B. A. S. Gustafson, "A generalized multiparticle Mie-solution: Further experimental verification," J. Quant. Spectrosc. Radiat. Transf. **70**, 395–419 (2001).
34. G. B. J. Dubelaar, and R. R. Jonker, "Flow cytometry as a tool for the study of phytoplankton," Scientia Marina. **64**(2), 135–156, (2000).
35. M . I. Mishchenko, L. D. Travis, and A. A. Lacis, *Scattering, Absorption and Emission of Light of Small Particles* (Cambridge University, 2002).
36. W. J. Clavano, E. S. Boss, and L. Karp-Boss, "Inherent optical properties of non-spherical marine-like particles - from theory to observation," Oceanography and Marine Biology. **45**, 1–38 (2007).
37. G. Chen, P. Yang, G. W. Kattawar, and M. I. Mishchenko, "Scattering phase functions of horizontally oriented hexagonal ice crystals," J. Quant. Spectrosc. Radiat. Transf. **100**, 91–102 (2006).
38. M. I. Mishchenko, and L. D. Travis, "Capabilities and limitations of a current FORTRAN implementation of the T-matrix method for randomly oriented, rotationally symmetric scatterers," J. Quant. Spectrosc. Radiat. Transf. **60**(3),

Optics EXPRESS

309–324 (1998).
39. Y.-l. Xu, "Electromagnetic scattering by an aggregate of spheres," Appl. Opt. **34**(21), 4573–4588 (1995).
40. A. R. Edmonds, *Angular Momentum in Quantum Mechanics* (Princeton University, 1957).
41. W. Yang, "Improved recursive algorithm for light scattering by a multilayered sphere," Appl. Opt. **42**(9), 1710–1720 (2003).
42. O. Peña, and U. Pal, "Scattering of electromagnetic radiation by a multilayered sphere," Computer Physics Communications. **180**(11), 2348–2354 (2009).
43. E. Aas, "Refractive index of phytoplankton derived from its metabolite composition," J. Plankton Res. **18**(12), 2223–2249 (1996).
44. C. D. Mobley, *Light and Water: Radiative Transfer in Natural Waters* (Academic, 1994).
45. K. L. Carder, R. D. Tomlinson, and C. F. Beadsley, "A technique for the estimation of indices of refraction of marine phytoplankters," Limnol. Oceanogr. **17**(6), 833–839 (1972).
46. A. Bricaud, A. L. Bédhomme, and A. Morel, "Optical properties of diverse phytoplanktonic species: Experimental results and theoretical interpretation," J. Plankton Res. **10**(5), 851–873 (1988).
47. A. Morel, and A. Bricaud, "Theoretical results concerning light absorption in a discrete medium, and application to specific absorption of phytoplankton," Deep-Sea Res. **28A**(11), 1375âĂŞ1393 (1981).
48. F. C. Stephens, "Variability of spectral absorption efficiency within living cells of Pyrocystis lunula (Dinophyta)," Marine Biology. **122**, 325–331 (1995).
49. R. J. Geider, and B. A. Osborne, "Light absorption by a marine diatom: experimental observations and theoretical calculations of the package effect in a small Thalassiosira species," Marine Biology. **96**(2), 299–308 (1987).
50. E. Charney, and F. S. Brackett, "The spectral dependence of scattering from a spherical alga and its implications for the state of organization of the light-accepting pigments," Archives of biochemistry and biophysics. **92**, 1–12 (1961).
51. J. L. Mueller, *The influence of phytoplankton on ocean color spectra* (Ph.D Thesis, Oregon State University., Corvallis, 1974).
52. H. R. Gordon, and T. Du, "Light scattering by nonspherical particles: Application to coccoliths detached from Emiliania huxleyi," Limnol. Oceanogr. **46**(6), 1438–1454 (2001).
53. J. M. Sullivan, M. S. Twardowski, J. R. V. Zaneveld, and C. C. Moore, "Measuring optical backscattering in water," A. Kokhanovsky, ed. *Light Scattering Reviews 7: Radiative Transfer and Optical Properties of Atmosphere and Underlying Surface* (Springer Praxis Books, 2013), pp. 189–224.
54. A. Quirantes, and A. V. Delgado, "Scattering cross sections of randomly oriented coated spheroids," J. Quant. Spectrosc. Radiat. Transf. **70**, 261–272 (2001).
55. A. Engel, "The role of transparent exopolymer particles (TEP) in the increase in apparent particle stickiness (alpha) during the decline of a diatom bloom," J. Plankton Res. **22**(3), 485–497 (2000).
56. A. Engel, "Distribution of transparent exopolymer particles (TEP) in the northeast Atlantic Ocean and their potential significance for aggregation processes," Deep-Sea Research Part I: Oceanographic Research Papers. **51**(1), 83–92 (2004).
57. S. G. Ackleson, and R. W. Spinrad, "Size and refractive index of individual marine participates: a flow cytometric approach," Appl. Opt. **27**(7), 1270–1277 (1988).
58. D. W. Mackowski, and M. Mishchenko, "A multiple sphere T-matrix Fortran code for use on parallel computer clusters," J. Quant. Spectrosc. Radiat. Transf. **112**(13), 2182–2192 (2011).
59. H. R. Gordon, "Backscattering of light from disklike particles: is fine-scale structure or gross morphology more important," Appl. Opt. **45**(27), 7166–7173 (2006).
60. M. Thyssen, S. Alvain, A. Lefèbvre, D. Dessailly, M. Rijkeboer, N. Guiselin, V. Creach, and L.-F. Artigas, "High-resolution analysis of a North Sea phytoplankton community structure based on in situ flow cytometry observations and potential implication for remote sensing," Biogeosci. **12**(13), 4051–4066 (2015).
61. M. Dugenne, M. Thyssen, D. Nerini, C. Mante, J.-C. Poggiale, N. Garcia, F. Garcia, and G. Grégori, "Consequence of a sudden wind event on the dynamics of a coastal phytoplankton community: an insight into specific population growth rates using a single cell high frequency approach," Frontiers in Microbiology. **5**, 1–14 (2014).

1. Introduction

Studies about the contribution of the phytoplanktonic compartment to the bulk Inherent Optical Properties (IOPs, [1]) increased over the last few years. These studies highlighted the importance of accounting for the heterogeneity/morphology of the phytoplankton cells when considering the scattering and more particularly the backscattering. Simulations were performed considering phytoplankton cells as two or three-layered spheres ([2–13]). Results indicated a higher backscattering coefficient or efficiency than predicted by the Mie theory, which considers particles as homogeneous spheres ([14–21]). Laboratory measurements confirmed multilevel light scattering by the cell, i.e. both by the outer cell membrane or frustule and the internal structure of the cell, as well as by its molecular structure ([22–28]). Many studies concluded

Optics EXPRESS

that it will be important, in the future, to investigate more precisely how the cells physiological conditions influence the scattering. Hobilabs Hydroscat, WET Labs ECO-BB or ECO-VSF are dedicated to routine *in situ* measurements of scattering at one or three scattering angles used for the assessment of the backscattering coefficient. These instruments can be deployed on a large variety of platforms at different time and space scales, relevant to the sediment or phytoplankton dynamics. However, they do not allow to accurately describe the contribution of each particulate compartment and to investigate the impact of the variations of the internal structure, except in the case of pure phytoplankton cultures. In this context, flow cytometers are valuable tools to analyze the individual scattering of particles and so move beyond the bulk information. They allow measurements of the sideward and forward scattering as well as fluorescence for each single particle going through the laser beam. Dubelaar *et al*., 1987 ([23]) pointed out the impact of a gas vacuole on the sideward and the forward scattering intensity from the Cytosense benchtop flow cytometer. This study illustrates potential applications of the Cytosense to analyze the impact of cell morphology on scattering. Green *et al*., 2003 ([29]) developed a method to derive the refractive index and the particle size combining flow cytometer measurements and simulations from Mie theory. This method was tested in New England continental shelf waters to quantify the contributions of phytoplankton and other particles to the inherent optical properties ([30]). They showed that the summed contributions of individual particle to phytoplankton absorption and particle scattering were close to values derived from bulk measurements. However, in some cases, as example during blooms conditions, their method leads to ambiguous estimates. They indicated clearly that there is a need for new approaches that overcome the limitations of Mie Theory.

More recently, Duforêt-Gaurier *et al*., 2015 ([31]) developed a new methodology to derive the forward, sideward and backward cross sections of individual particles from measurements of the Cytosense. This method is valid for homogeneous and heterogeneous spherical or non spherical particles contrary to previous methodologies deriving particle diameter and complex refractive index but assuming particles as homogeneous spheres. The method was successfully tested on different NIST (National Institute of Standards and Technology) traceable beads. In their discussion, the authors pointed out the need to test the method on more complex natural particles and more particularly, in the framework of marine optics, on phytoplankton cells. In the continuity of the Duforêt-Gaurier *et al*., 2015's work, the objectives of the present study were to apply the methodology on phytoplankton cells to test its robustness on natural particles and so identify and analyze its potential errors. For that purpose, the method was tested on two species, *Thalassiosira pseudonana* (a diatom) and *Chlamydomonas concordia* (a flagellate green algae), during a complete life cycle. These two species are very distinct from a morphological point of view. *Thalassiosira pseudonana* stands for particles with a silica wall and single cells are in most cases cylindrical. *Chlamydomonas concordia* is a small ovoid and may potentially form aggregates during the experience. Moreover, the cell size, the shape, the thickness of the silica wall, the Chlorophyll$_a$ by cell or the aggregate configurations, change during the life cycle; it permits to test the method on an large set of targets.

The proposed study is divided in third steps. First, before testing the method on natural particles, we have to address an issue pointed by Duforêt-Gaurier *et al*., 2015 in their discussions. Indeed, for particles of all shapes and all sizes, the polarization of the incident laser beam may impact the signal scattered by the particle and recorded by the detectors. It results that the Cytosense could still be used to measure the sideward and forward cross sections but not anymore to derive the backscattering coefficient. For that purpose, numerical computations have been realized for non-spherical particles (spheroids and aggregates) with the oriented T-matrix code ([32]) and the Generalized Multiparticle Mie-solution (GMM) code ([33]) to examine theoretically the impact of the polarization on the Cytosense signal. Second, the comparison exercise was realized to quantify the accuracy of the Cytosense estimates over phytoplankton

Optics EXPRESS

cells cultures. As no database of the sideward and the forward cross sections is available in the literature, the Cytosense estimates were compared with radiative transfer computations. 590,000 simulations were carried out to include homogeneous and layered sphere models representing the optical properties of a large diversity of phytoplankton cells. The backward cross section and backward efficiency factor estimates were compared with available *in situ* data found in the literature. Third, after the analysis of the sources of errors, few possible improvements were proposed in the conclusions. Considering the objectives cited above, the present study can be considered as technical. However, such work is mandatory before considering any potential utilization of the Cytosense in the framework of marine optics.

2. Material and method

2.1. Phytoplankton cultures

Monospecific cultures *Thalassiosira pseudonana* (THAL) and *Chlamydomonas concordia* (CHLAM) were obtained from the Roscoff Culture Collection (RCC, http://roscoff-culture-collection.org). THAL is a diatom and stands for particles with a silica wall and CHLAM is a flagellate green algae. CHLAM and THAL were maintained in monospecific conditions in a f/2 medium at 17 °C, under a photon flux density of about 100 μmol.photons.m^{-2}.s^{-1} with a 12:12h light:dark cycle. They were grown in batch mode during 15 days to obtain 4.5 L of culture. One day before the beginning of the microcosm experiment, the 4.5 L of culture were added to 60 L of fresh f/2 medium. A volume of 60 L was required to realize a daily sampling for biogeochemical analysis, while maintaining a sufficient depth ($\geq$ 25 cm) for the optical measurements. The cultures were maintained under a surface illumination of 200 μmol.photons.m^{-2}.s^{-1}. The 12:12h light:dark cycle and the temperature of 17 °C were maintained. A continuous agitation was applied to homogenize the medium and to avoid the formation of chains. The salinity of the four batches was between 29.1-29.7.

2.2. Flow cytometry

In this study, we used the Cytosense (CytoBuoy b.v., NL ; http://www.cytobuoy.com) of the PRECYM flow cytometry platform of the Mediterranean Institute of Oceanography (MIO; http://precym.mio.univ-amu.fr). The Cytosense is a benchtop pulse-shape flow cytometer designed for the observation of phytoplankton cells. It counts and analyzes particles with diameters between 1 and 800 μm. The sample intake speed is of 3 μl.s^{-1}. Particles in suspension are injected into a free carrying sheath fluid, that narrows down the suspension into a thin line of fluid. The velocity of the particle suspension is governed by the sheath flow rate, factory set at about 2.2 m.s^{-1}. The particles are aligned along the path of the fluid, which is perpendicular to the direction of the laser beam. Considering the design of the Cytosense and the analysis conditions, we assume that for non-spherical particles, the particle longer axis is vertically oriented perpendicularly to the laser beam. Particles flow one by one, through, the focused laser beam. The laser is a Coherent Inc. Saphyre, 488 nm, vertically polarized, with a power of 15 mW and a beam diameter of 0.7 mm. The Cytosense beam shaping, converts the single beam in two horizontally displaced beams with polarization of +45° and -45° relative to the original polarization of the laser beam. The superposition of these two Gaussian beams, with partly overlapping light distributions provides a flat light distribution over the sensing zone of the detectors. With this double beam solution, particles are illuminated by radiation coming from the +45° and -45° polarized beams. If a particle is flowing in the middle of the flow cell, the light scattered by the particle contains equal amounts of both polarization states. If a particle is flowing through the combined irradiance profile of both laser beams at some distance d away from the middle, the scattered light will contain proportionally more light from one beam than from the other one with the other polarization state (see Fig. 1 in Duforêt *et al.*, 2015). The forward scattered light (FSC) is collimated and directed onto two PIN photodiode detectors, one

Optics EXPRESS

with a +45° angle polarizer in front of the photodiode and one with a -45° angle polarizer. In the analysis software, the signals from the two detectors are summed together to provide the forward scattering of each particle. The collection solid angle of the forward scatter detectors starts at ca. 2°, going up to ca. 15°. The sideward scattered light (SSC), together with the fluorescence emission, is collected at 90° (with a solid angle between ca. 45° and ca. 135°) by series of photomultiplier tubes, using a set of dichroic mirrors and band pass filters. The fluorescence emitted by photosynthetic pigments in algal cells is detected at three different spectral bands. The resulting signatures, which are displayed as red and orange fluorescence respectively, assist in determining the pigment type of each particle. The yellow fluorescence detector is specific to stains of certain calibration beads. Digital data acquisition is initiated as the particle enters into the laser beam and is terminated when the particle is no longer detected. The data recording is done at a frequency of 4 MHz. Data recording was triggered by the SSC signal (15 mV). This trigger permitted to remove a part of the instrumental electronical noise as the smallest particles.

The proprietary Cytoclus software (CytoBuoy b.v., NL) was used to manually analyze the data ([34]). It enables the clustering of data points representing cells having similar optical properties, constituted by their forward and sideward scattering, and their various fluorescence signals. The clustering uses up to 10 simple mathematical signal descriptors of each available detector signal (for example, length, height, center of gravity, asymmetry, number of humps...). The various clusters are selected manually by drawing gates in correlated bivariate scatter plots. This combines objective factors from the cytograms and subjective considerations linked to the operator expertise. Moreover, an “image-in-flow" device, mounted in the Cytosense, takes pictures of cells within a predefined zone of interest.

2.3. Theoretical considerations

Light scattering is produced by the presence of an object (such as a particle) with a refractive index different from that of the surrounding medium. The refractive index is expressed in a complex form as $m(\lambda) = m_r(\lambda) + i\, m_i(\lambda)$, where λ is the wavelength of the radiation , relative to the medium. The real part determines the phase velocity of the wave ($v(\lambda) = c/m_r(\lambda)$) with c the speed of light in a vacuum. The imaginary part represents the absorption of light as it propagates through the particle with $a_{cm}(\lambda)$ the absorption coefficient of the cellular material equal to $4\pi\, m_i(\lambda)/\lambda$. The direction of propagation of a traverse electromagnetic wave is specified by a unit vector $\mathbf{n}$ or, equivalently, by a couple (θ, ϕ), where $\theta \in [0, \pi]$ is the polar (zenith) angle and $\phi \in [0, 2\pi]$ is the azimuth angle ([35]). The angular distribution and polarization of the scattered field depend on the polarization, directional characteristics of the incident field, and on the properties of the particle as its size parameter ($s(\lambda) = \pi D/\lambda$ with D its diameter), its shape, composition, structure and orientation. The single scattering of light by an object is described by the scattering cross section $\sigma_{sca}(\lambda)$ (units, m^2) and the phase matrix $\tilde{Z}(\lambda, \mathbf{n}_{sca}, \mathbf{n}_{inc})$ with $\mathbf{n}_{inc}$ and $\mathbf{n}_{sca}$ the direction of the incident and scattered radiation. The scattering cross section is defined by [35]:

$$\sigma_{sca}(\lambda) = \frac{r^2}{I_{inc}(\lambda, \mathbf{n}_{inc})} \int_{4\pi} d\mathbf{n}_{sca} I_{sca}(\lambda, \mathbf{n}_{sca}), \tag{1}$$

with r the distance from the particle, I_{sca} is the incident intensity. The scattered intensity I_{sca} is defined from the incident Stokes vector, from the incident radiation, as follows:

$$I_{sca} = \frac{1}{r^2}(Z_{11} I_{inc} + Z_{12} Q_{inc} + Z_{13} U_{inc} + Z_{14} V_{inc}). \tag{2}$$

Optics EXPRESS

Note that, in Eq. (2), the spectral and directional dependencies are omitted for clarity. The phase matrix of a particle is defined by:

$$\tilde{Z} = \begin{pmatrix} Z_{11} & Z_{12} & Z_{13} & Z_{14} \\ Z_{21} & Z_{22} & Z_{23} & Z_{24} \\ Z_{31} & Z_{32} & Z_{33} & Z_{34} \\ Z_{41} & Z_{42} & Z_{43} & Z_{44} \end{pmatrix}. \tag{3}$$

As previously, λ, $\mathbf{n}_{inc}$ and $\mathbf{n}_{sca}$ have been omitted for clarity. For a spherical particle, we assume that the incident light propagates along the positive z-axis of the laboratory reference frame (L{X, Y, Z}) and that the XZ-plane with X≥0 is the meridional plane of the incident beam. In this case, the Stokes vector of the scattered beam can be computed with respect to its own reference plane and the phase matrix can be written as:

$$\begin{aligned} \tilde{Z}(\lambda, \mathbf{n}_{sca}, \mathbf{n}_{inc}) &= \tilde{F}(\lambda,\theta)\tilde{L}(\phi) \\ &= \begin{pmatrix} F_{11}(\lambda,\theta) & F_{12}(\lambda,\theta)cos2\phi & -F_{12}(\lambda,\theta)sin2\phi & 0 \\ F_{12}(\lambda,\theta) & F_{22}(\lambda,\theta)cos2\phi & -F_{22}(\lambda,\theta)sin2\phi & 0 \\ 0 & F_{33}(\lambda,\theta)sin2\phi & F_{33}(\lambda,\theta)cos2\phi & F_{34}(\lambda,\theta) \\ 0 & -F_{34}(\lambda,\theta)sin2\phi & -F_{34}(\lambda,\theta)cos2\phi & F_{44}(\lambda,\theta) \end{pmatrix}, \end{aligned} \tag{4}$$

with $\tilde{L}(\phi)$ the rotation matrix (see Fig. 4.6 p. 96 in [35]). The scattering matrix $\tilde{F}(\lambda,\theta)$ is independent on the particle orientation and is constant with respect to the azimuth. Combining Eq. (1)–(4), the sideward cross section is written as follows:

$$\sigma_{SSC}(\lambda) = 2\pi \int_{45^o}^{135^o} F_{11}(\lambda,\theta)sin(\theta)d\theta. \tag{5}$$

Integrating $F_{11}(\lambda,\theta)$ over the backward hemisphere gives the backscattering cross section:

$$\sigma_{b_b}(\lambda) = 2\pi \int_{90^o}^{180^o} F_{11}(\lambda,\theta)sin(\theta)d\theta. \tag{6}$$

For a non spherical particle in a fixed orientation, Eq. (4)–(6) are no more valid. Indeed, $\tilde{F}(\lambda,\theta)$ becomes dependent of the particle orientation and depends on the azimuth angle. Considering the Cytosense design, ignoring a multiplication factor, Duforêt-Gaurier *et al.*, 2015 found that the Stokes parameters of the incident light are defined by (I,0,(2α-1)I,0) with α the fraction of light coming from the +45° polarized beam. Duforêt-Gaurier *et al.*, 2015 noted that as the forward detected signal is the sum of the intensity of the two forward detectors, it is proportional to:

$$Z_{11}(\lambda,\theta,\phi)I + (2\alpha - 1)Z_{13}(\lambda,\theta,\phi)I, \tag{7}$$

with Z_{11} and Z_{13} the elements of the phase matrix (Eq. (3)). For the sideward detector with no polarizer, the detecting signal (SSC) is also given by Eq. (7). Thus, the sideward cross section can be written as follows:

$$\sigma_{SSC}(\lambda) = \int_{0^o}^{360^o} \int_{45^o}^{135^o} (Z_{11}(\lambda,\theta,\phi) + (2\alpha - 1)Z_{13}(\lambda,\theta,\phi))sin(\theta)d\theta d\phi. \tag{8}$$

The same equation can be written for the backward cross section by changing the limits of integration ([90°,180°] instead [45°,135°]). The efficiency factor Q is the ratio of the cross

Optics EXPRESS

section area to the geometrical cross section (< G >) ([18]):

$$Q_{SSC} = \frac{4\sigma_{SSC}}{\pi D^2}. \quad (9)$$

The same equation can be written for the backward scattering with b_b instead of SSC. For non-spherical particles, D is the surface or volume equivalent sphere diameter.

2.4. Radiative transfer computations

In this study, four free public access radiative transfer codes were used for computing the scattering properties of homogeneous spheres, layered spheres, aggregates and non spherical particles in fixed orientation. Radiative transfer computations were carried out considering the wavelength of the incident radiation equal to 488 nm and the refractive index of water equal to 1.334 ([18]).

T-Matrix

The T-matrix code ([32]) is one of the most widely used tools for rigorously computing of electromagnetic scattering by non spherical particles. It is limited to particles with a phase shift parameter ($\rho = 2s(\lambda)(m_r - 1)$) up to about 10 ([36]). The code is largely used for rotationally symmetric particles (spheroids or cylinders) in random orientations but a version exits also for rotationally symmetric particles in a fixed orientation. The latter is used, in this study, to simulate the scattering of non spherical particles flowing through the laser beam.

To describe the scattering of a non spherical particle in a fixed orientation, we have to define the directions of incident and scattered radiations and the orientation of the particle with respect to the reference frame. The laboratory reference frame, named L, is a right-handed Cartesian coordinate system with orientations (X, Y, Z) fixed in space. To specify the orientation of the particle, we introduce the particle reference frame, named P, with the (X_p, Y_p, Z_p) axis. The reference frames L and P have the same origin inside the particle. It is convenient to choose the direction of the Z_p axis such as it corresponds to the revolution axis of the particle, and to choose the Z axis along the propagation direction of the incident radiation ([32, 37]) (Fig. 1). The orientation of P with respect to L is specified by three Euler angles (α, β and γ) that transform L{ X,Y,Z } into P{ X_p,Y_p,Z_p } ([32]). Considering the orientations of the particles (Fig. 1), the Euler angles are equal to (0°,90°,0°) for prolate particles (EPS<1, with EPS the ratio of the diameter to the particle length, [38]) and (0°,0°,0°) for oblate particles (EPS>1). The code inputs are: the Euler angles, the refractive index of the particle, the equivalent size diameter and the EPS of the particle.

Generalized multiparticle Mie-solution

Computations of aggregates in fixed orientation are performed with the Generalized Multiparticle Mie-solution (GMM) code ([33]). The GMM's code, is an extension of the Mie solution from a single particle to the multi-particle case. The scattering formulation and numerical techniques used in this code are beyond the scope of this study but are described in [39] or more recently in [33]. The direction of propagation of the incident plane wave defines the positive Z-axis and the scattering plane is defined by the X-Z plane. Considering the configuration of the clusters (Table. 1) and following the convention used by Edmonds, 1957 ([40]), the Euler angles are: α = 0°, β = 90° and γ = 0°. In addition, the code inputs are the position (x,y,z), the size and the refractive index of each sphere which composes the aggregate.

ScattnLay

The ScattnLay code constitutes an alternative to the Mie theory to simulate the optical properties of phytoplankton cells accounting for their structural variability. It considers a particle as a

Optics EXPRESS

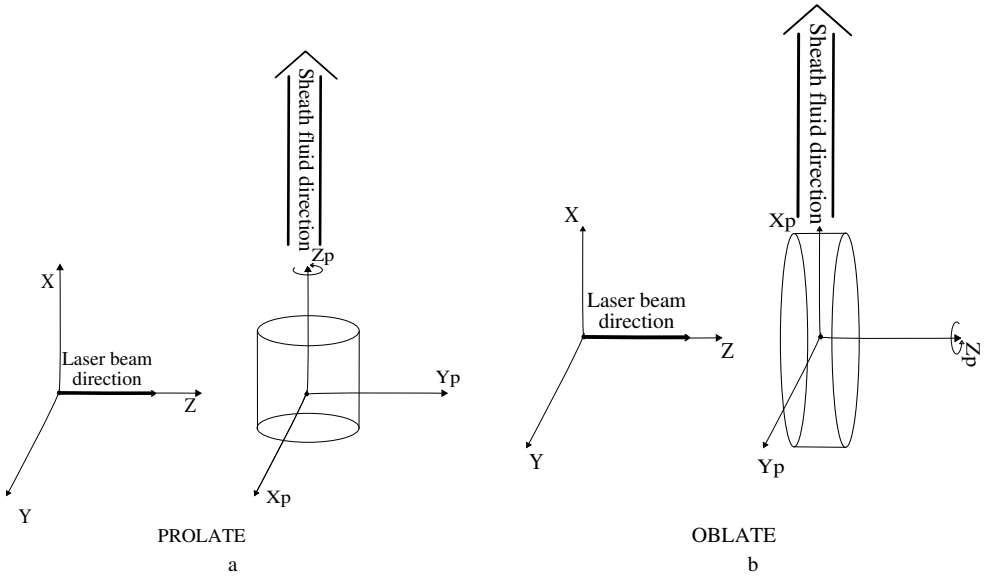

Fig. 1. Coordinate systems defined for a) a prolate and b) an oblate cylinder, incidence geometry and scattering configuration. L{ X,Y,Z } is the laboratory reference frame with Z-axis along the propagating direction of the incident beam (bold arrow). P{ X_p,Y_p,Z_p } is the particle reference frame. The particle flows up following the sheath fluid.

multi-layered sphere. The code is based on calculations of Mie scattering coefficients and efficiency factors combined with a standard solution of the scattering amplitude functions. In fact, the solution of the scattering by concentric layered spheres consists in expressing the electromagnetic fields in each layer l in terms of appropriate sets of spherical wave functions (see details in [41] and [42]). The code is efficient, numerically stable, and accurate for a large range of size parameters ($s(\lambda)$ up to 350) and refractive index. Each j-th layer, with j = 1, 2, ..., K, is characterized by its complex refractive index relative to the medium ($m_j = m_{rj} + im_{ij}$) and by its size parameter s_j. The letter K stands for the number of layers constituting the cell.

2.5. Numerical databases

Database DTB1

A numerical database named DTB1 includes computations of aggregates and oblate or prolate cylinders in a fixed orientation. Firstly, radiative transfer simulations were performed with the T-Matrix algorithm for fixed oriented particles. We simulated monodispersed prolate and oblate cylinders with surface equivalent sphere diameter (D_e) between 3 and 7 μm (increment of 1) and EPS between 0.6 and 1.6 (increment of 0.1). These D_e and EPS ranges were observed on *Thalassiosira pseudonana* from scanning electron microscopy. We used a mean complex refractive index for phytoplankton cells of $m = 1.05 + i0.01$ ([36]).

Secondly, computations were performed for 17 different cell aggregates. They were composed of 2, 3, 4, 5, 8 and 9 spheres arranged as indicated in Table 1. Each sphere composing the cluster had a diameter of 4 μm and a refractive index of : $m = 1.05 + i0.01$. In the following, clusters are named C_2, C_{3a},C_{3b}, C_{4a} to C_{4d}, C_5, C_{8a} to C_{8h} and C_9; the number indicates the number of spheres composing the cluster and the letter identifies a given configuration for the position of the spheres. The SEM micrographs of *Chlamydomonas concordia* showed that the most frequently encountered clusters correspond to the C_2, C_{3a}, C_{3b}, C_5 and C_9. Note that, all

Optics EXPRESS

Table 1. Position (x_p, y_p, z_p) of each sphere composing the simulated aggregate in the particle frame. C stands for Cluster, the number indicates the number of spheres composing the aggregate and the letter stands for a given configuration

Cluster name	Sphere position in the particle frame								
	S_1	S_2	S_3	S_4	S_5	S_6	S_7	S_8	S_9
C_2	{0,0,0}	{4,0,0}							
C_{3a}	{0,0,0}	{4,0,0}	{-4,0,0}						
C_{3b}	{3.46,0,0}	{0,2,0}	{0,-2,0}						
C_{4a}	{0,2,2}	{0,-2,-2}	{0,-2,2}	{2.83,0,0}					
C_{4b}	{0,2,-2}	{0,-2,-2}	{0,-2,2}	{2.83,0,0}					
C_{4c}	{0,2,-2}	{0,2,2}	{0,-2,2}	{2.83,0,0}					
C_{4d}	{0,2,-2}	{0,2,2}	{0,-2,-2}	{2.83,0,0}					
C_5	{0,2,-2}	{0,2,2}	{0,-2,-2}	{0,-2,2}	{2.83,0,0}				
C_{8a}	{0,2,2}	{0,-2,-2}	{0,-2,2}	{-4,2,2}	{-4,2,-2}	{-4,-2,-2}	{-4,-2,2}	{-6.83,0,0}	
C_{8b}	{0,2,-2}	{0,-2,-2}	{0,-2,2}	{-4,2,2}	{-4,2,-2}	{-4,-2,-2}	{-4,-2,2}	{-6.83,0,0}	
C_{8c}	{0,2,-2}	{0,2,2}	{0,-2,2}	{-4,2,2}	{-4,2,-2}	{-4,-2,-2}	{-4,-2,2}	{-6.83,0,0}	
C_{8d}	{0,2,-2}	{0,2,2}	{0,-2,-2}	{-4,2,2}	{-4,2,-2}	{-4,-2,-2}	{-4,-2,2}	{-6.83,0,0}	
C_{8e}	{0,2,-2}	{0,2,2}	{0,-2,-2}	{0,-2,2}	{-4,2,-2}	{-4,-2,-2}	{-4,-2,2}	{-6.83,0,0}	
C_{8f}	{0,2,-2}	{0,2,2}	{0,-2,-2}	{0,-2,2}	{-4,2,2}	{-4,-2,-2}	{-4,-2,2}	{-6.83,0,0}	
C_{8g}	{0,2,-2}	{0,2,2}	{0,-2,-2}	{0,-2,2}	{-4,2,2}	{-4,2,-2}	{-4,-2,2}	{-6.83,0,0}	
C_{8h}	{0,2,-2}	{0,2,2}	{0,-2,-2}	{0,-2,2}	{-4,2,2}	{-4,2,-2}	{-4,-2,-2}	{-6.83,0,0}	
C_9	{0,2,-2}	{0,2,2}	{0,-2,-2}	{0,-2,2}	{-4,2,2}	{-4,2,-2}	{-4,-2,-2}	{-4,-2,2}	{-6.83,0,0}

the clusters presented a symmetric plan except C_{4a-d} and C_{8a-h}.

Database DTB2

A second database named DTB2 is made up of 590,000 computations, carried out with the ScattnLay code. An exhaustive review of the internal structure of phytoplankton cells was performed by Bernard *et al*., 2009 ([8]). We used this review to define the relevant refractive indices and the relative proportions of the different layers. Homogeneous spheres are used as the reference model to discuss the impact of the cell heterogeneity. The values of the real part of the refractive index range from 1.03 to 1.09 with 0.01 increments. Such values corresponds to cells with a high water content ([16, 20, 43–46]). The imaginary part spans from 0.001 to 0.015 in increments of $2.857.10^{-4}$. The lower limit represents weakly absorbing cells, whereas the upper limit represents the extremely absorbing cells having photosynthetic pigments ([6, 14, 15, 20, 47]). As Bernard *et al*., 2009, we simulated a two-layered sphere model composed of an inner layer, the cytoplasm (cyto) and an outer layer, the chloroplast (chl). The cytoplasm is non pigmented and weakly absorbing as it is mostly composed of water ([2, 7, 8, 48]). The chloroplast, constituted of pigment-proteins, responsible for photosynthesis, is extremely absorbing ([47, 49]). The relative proportions are $60\%_{cyto}$-$40\%_{chl}$, $70\%_{cyto}$-$30\%_{chl}$ and $80\%_{cyto}$-$20\%_{chl}$. In addition, cells with a silica wall (as THAL) are simulated as three-layered spheres. The cytoplasm is the inner layer, the chloroplast is the middle layer and the non-absorbing silica wall is the outer layer ([43]). The relative volumes are $80\%_{cyto}$-$18.625\%_{chl}$-$1.375\%_{Si}$ or $80\%_{cyto}$-$15\%_{chl}$-$5\%_{Si}$. The relative volume of the silica wall (V_{Si}) is measured from SEM micrographs. Arbitrarily, we chose the fourth day of the experiment to measure V_{Si}. The mean value, equal to $1.375\% \pm 0.34$, is considered as a mean reference value. The V_{Si} of 5% is considered as an extreme case as in Kitchen *et al*., 1992 ([3]). The real part of the cytoplasm refractive index ($m_r(cyto)$) is fixed to 1.02. This value falls within the interval of referenced indices ($1.015 \leq m_r(cyto) \leq 1.035$; [2, 3, 5, 7, 8, 12, 50]). The $m_i(cyto)$ is fixed to 2.0739×10^{-4} (according to Eq. (22) in [8]). The

Optics EXPRESS

value of $m_r(Si)$ is equal to 1.07 or 1.09 (as given in [3,43,49,51]) and $m_i(Si)$ is of 0.0001 or 0.0 (as in [3,15,51]). Concerning the chloroplast, $m_r(chl)$ and $m_i(chl)$ are calculated according to the Gladstone and Dale formula ([43]):

$$\sum_j m_j v_j = m_m, \tag{10}$$

where m_j and v_j are the complex refractive index and the relative volume of the j-th layer, and m_m the complex equivalent refractive index ($m_m = m_{rm} + im_{im}$). Note that, $m_r(chl)$ and $m_i(chl)$ are selected so that the equivalent m_{rm} and m_{im} of phytoplankton cells fall within the m_{rm} and m_{im} ranges of homogeneous spheres. The knowledge of the complex equivalent refractive index is useful to compare the simulations of heterogeneous and homogeneous spheres or the simulations of heterogeneous spheres among themselves, regardless the number of layers and the relative proportion of each layer. The $m_r(chl)$ values above 1.23 and under 1.06 were disregarded because they do not fall within the range of referenced values ([8] and references there in). It results that the upper and lower limits of the equivalent m_{rm} are 1.04-1.08 for $70\%_{cyto}$-$30\%_{chl}$ spheres, 1.03-1.06 for $80\%_{cyto}$-$20\%_{chl}$ spheres and $80\%_{cyto}$-$18.625\%_{chl}$-$1.375\%_{Si}$ spheres, and 1.03-1.05 for $80\%_{cyto}$-$15\%_{chl}$-$5\%_{Si}$ spheres (in increments of 0.01). Diameters were fixed to enclose the range of size as observed from the Cytosense. Remind that, the Cytosense provides estimates of the particle length. For rather spherical particles as THAL and CHLAM, we assume that the length is equal to the diameter of the particle (see section 3.6). Simulations were performed for D between 1 to 40 μm (0.166 μm increment).

3. Results

3.1. Morphology of the species

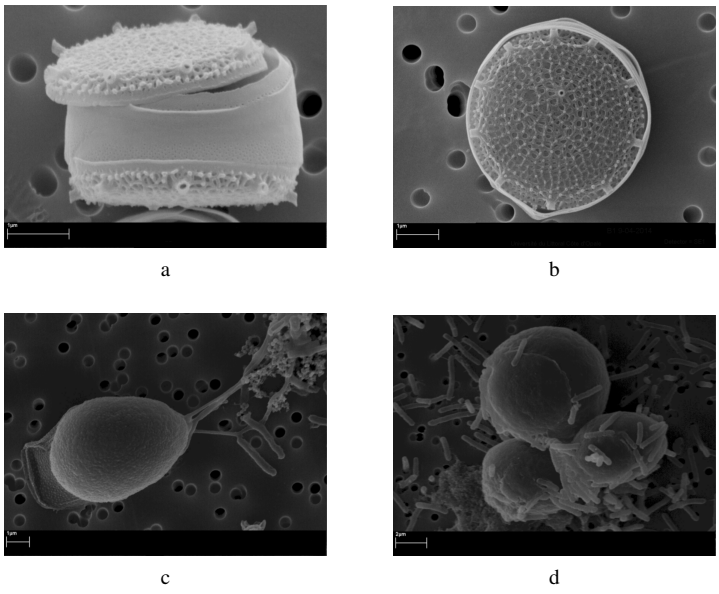

Fig. 2. Scanning electron microscopy images of a) side and b) top view of *Thalassiosira pseudonana*; c) single cell of *Chlamydomonas concordia*; and d) aggregate form of *Chlamydomonas concordia* (for the fourth day of the experiment).

The morphologies of THAL and CHLAM are different as shown on the SEM images (Fig.

Optics EXPRESS

2). THAL (Figs. 2a and 2b) is a species of marine diatom characterized by a silica wall. SEM micrographs showed that THAL shape was cylindrical with an surface equivalent diameter D_e between 3 and 7 μm. Over the whole experiment, the mean EPS values varies between 0.6 and 1.6. We note an aggregate formation at the end of the experiment (see section 3.6). CHLAM is a flagellate and contrary to THAL, does not have a silica wall. The CHLAM cell is an ovoid with a flagellum (Fig. 2c). CHLAM cells can form aggregates as shown on Fig. 2d. The surface equivalent diameter was between 2 and 34 μm and the mean EPS was between 0.6 and 0.7.

3.2. Impact of the polarization

In this paper, the methodology of Duforêt-Gaurier *et al*., 2015 is used to derive the forward (σ_{FSC}), sideward (σ_{SSC}) and backward (σ_{b_b}) cross sections (μm^2). First, the weighting functions for the forward and sideward detectors, are calculated to convert numerical counts into cross sections. Then, the σ_{SSC} is converted into σ_{b_b} using the theoretical relationship defined in Duforêt-Gaurier *et al*., 2015. As shown in the section 2.3 and as pointed out by the authors in their conclusions, for oriented non-spherical particles, the signal measured by the Cytosense depends on the first element of the scattering matrix Z_{11} but can also depend on Z_{13}. In this case, the weighting functions of the forward and sideward detectors are still valid but the theoretical relationship to derive σ_{b_b} from σ_{SSC} can not be applied anymore. Indeed, this relationship was established from computations according to Eq. (5) without considering Z_{13}. For small cylinders, ovoids or aggregates as THAL and CHLAM, it is important to check if Z_{13} has a significant impact on the sideward and/or backward cross sections (Eq. (8)). For this purpose, the DTB1 database is used (see section 2.5). Figure 3 shows the ratio Z_{13}/Z_{11} (%) as a function of the azimuth and zenith angles for two cylinders with $D_e = 6$ μm. The first one is a prolate with an EPS of 0.7 (Fig. 3a) and the second one is an oblate with an EPS of 1.3 (Fig. 3b). The Z_{13}/Z_{11} ratio (absolute value) varies between 0% and ±100%. It shows that, in some cases, Z_{13} is not negligible as compared to Z_{11}. The ratio Z_{13}/Z_{11} shows antisymmetric features. The values observed for ϕ between [0°, 90°[(whatever θ) are positive, whereas the values between [90°, 180°[are negative and are their exact opposite. The same observation can be done by comparing Z_{13}/Z_{11} for ϕ between [180°, 270°[and between [270°, 360°[. The antisymmetrical features are due to Z_{13} and not Z_{11}. Indeed, we studied the Z_{11} values (not show here) as function of θ and ϕ as the same way as for Z_{13}/Z_{11}. We noticed that Z_{11} presents some symmetrical features: values between [0°, 90°[are identical to values between [90°, 180°[. Similarly, values between [180°, 270°[are identical to values between [270°, 360°[. The Z_{11} and Z_{13} functions are studied as a function of the zenith angle after the integration over the azimuth angle (not shown here). Due to the antisymetrical features, $Z_{13}(\theta)$ is null whatever θ, contrary to $Z_{11}(\theta)$. $Z_{11}(\theta)$ displays, as expected, a highly peaked forward scattering and a rather flat broad minimum for medium scattering angles following by an increase at backward angles. It results that the sideward or backward cross section depends only on Z_{11}. Note that, same conclusions are observed for all of the other simulated cylinders. We supposed that Z_{11} displays symmetrical features and Z_{13} antisymmetrical features because cylinders are bisected by a plane of symmetry. To validate this hypothesis, we studied the Z_{13}/Z_{11} ratio for aggregates with a plane of symmetry (C_5 and C_9) and aggregates without a plane of symmetry (C_{4a-d} and C_{8a-h}). Figure 4 displays only the ratio Z_{13}/Z_{11} (%) for the clusters C_9 and C_{8a}. For C_9, Z_{13}/Z_{11} and Z_{11} shows antisymmetrical and symmetrical features, as previously observed for the cylinders. On the contrary, for C_{8a}, the values of Z_{13}/Z_{11} for ϕ between [0°, 90°[are not strictly the opposites of the values between [90°, 180°[(see black circles on the Fig. 4b). The same remark can be done comparing Z_{13}/Z_{11} for ϕ [180°, 270°[and [270°, 360°[. Figure 5 displays Z_{11} and Z_{13} as a function of the zenith angle for the C_9 and C_{8a} aggregates after the integration over ϕ. Please note that the absence of values on the Z_{13} curve corresponds to negative values, not plotted using a logarithmic scale. The integrated Z_{11} values are similar for C_9 and C_{8a}. As for the cylinders, the integrated Z_{13} values

Optics EXPRESS

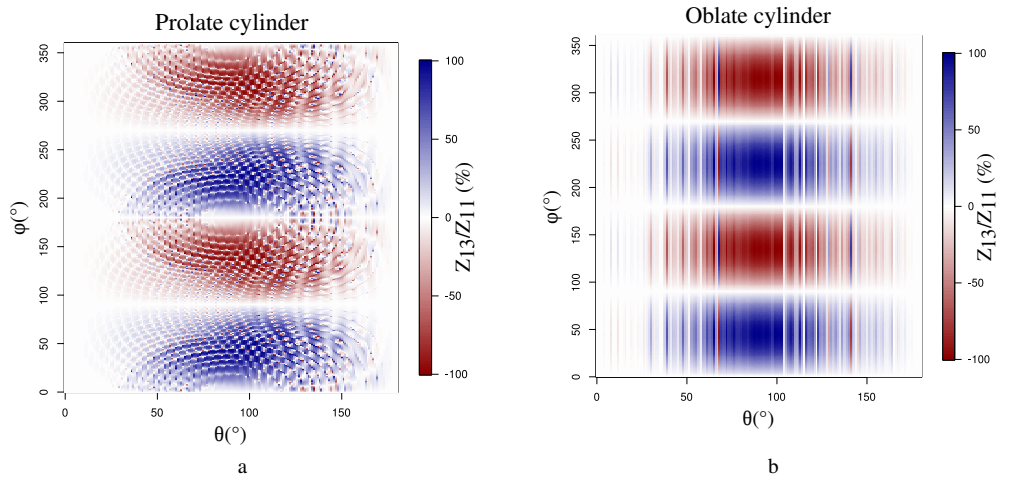

Fig. 3. Color contour plots Z_{13}/Z_{11} (%) , vs the zenith and the azimuth angles for monodisperse a) prolate (EPS = 0.7) and b) oblate (EPS = 1.3) cylinders in a fixed orientation with an surface equivalent sphere radius of 3 μm in fixed orientation. The refractive index is 1.05 + i0.01.

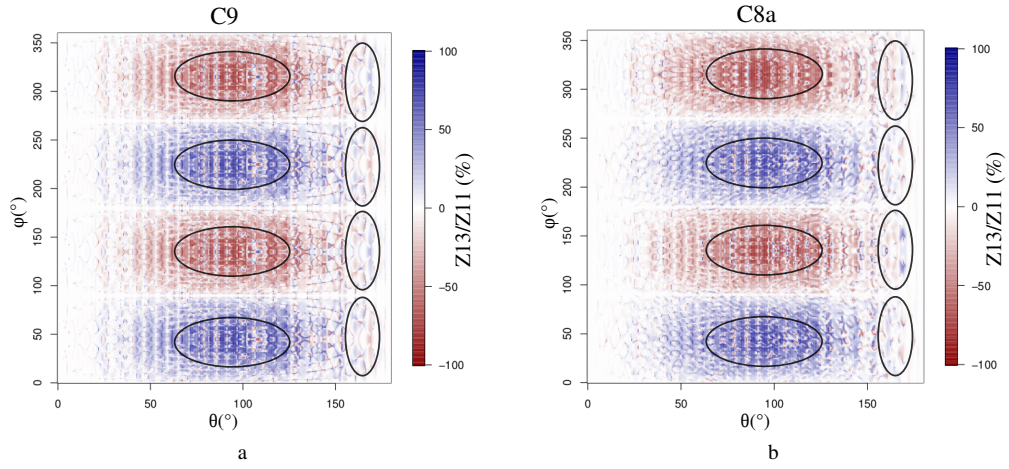

Fig. 4. Color contour plots Z_{13}/Z_{11} (%) , vs the zenith and the azimuth angles for monodisperse aggregate for cluster a) C_9 and b) C_{8a} in a fixed orientation. The diameter and refractive index of each sphere are 4 μm and 1.05 + i0.01, respectively.

are null for C_9. On the contrary, and as expected, the integrated Z_{13} values are not null for C_{8a}. It results that Z_{13} impacts the sideward and backward cross sections. Considering the extreme case with $\alpha = 1$, which means that the particles is totally polarized at +45°, we quantified the impact of Z_{13} on σ_{SSC} and σ_{b_b} for clusters C_{4a-d} and C_{8a-h}. Results showed that the absolute relative differences are not negligible (Table 2). We note that for other value of α, excepted if $\alpha = 0$, the impact of Z_{13} is lower. Computation results for aggregates (C_{4a-d} and C_{8a-h}) fall within the dispersion observed around the regression established in Duforêt-Gaurier *et al.*, 2015. It results that the impact of Z_{13} does not exceed *a priori* the variability due to the refractive index

Optics EXPRESS

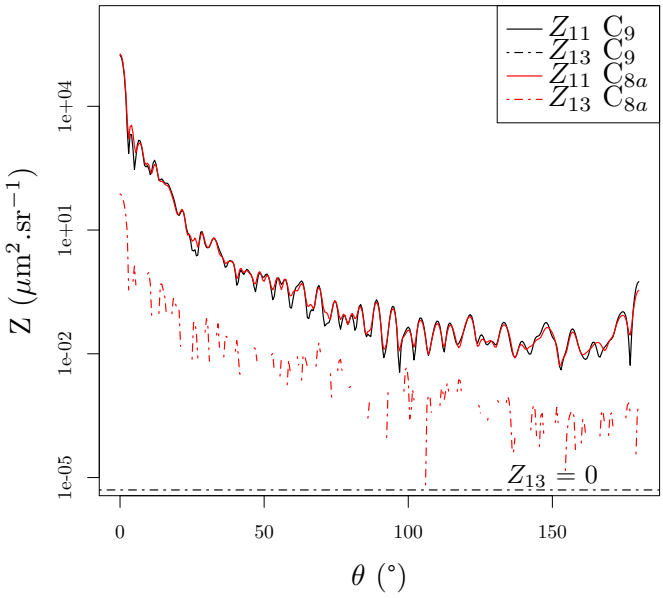

Fig. 5. Elements Z11 (solid lines) and Z13 (dotted lines) of the phase matrix (after integration according to the azimuth angle) as a function of the zenith angle for the cluster C_{8a} and C_9.

Table 2. The mean absolute relative difference (%) between the σ_{SSC} or σ_{b_b} values obtained considering the Z_{13} term and without considering Z_{13} for different aggregate configurations.

Variable	MARD (%)	
	C_{4a-d}	C_{8a-h}
σ_{SSC}	13.7	7.4
σ_{b_b}	24.3	9.7

or the particle size. For this reason, we will consider that the established relationship is valid despite the impact of the polarization. Moreover, the SEM micrographs showed that in most cases, aggregates present a plane of symmetry.

3.3. *The cytosense measurements*

Cytosense measurements have been conducted over the four batches. From each Cytosense analyze, living phytoplankton cells and degenerated cells were identified separately from their optical properties and fluorescence signals. A distinction was also made between clusters corresponding to living cells of THAL and clusters corresponding to living cells of CHLAM, to detect a possible contamination. The forward (FSC) and sideward scattering (SSC) signals were converted into forward (σ_{FSC}) and sideward (σ_{SSC}) scattering cross sections according to the Duforêt-Gaurier *et al.*, 2015's methodology. The probability density functions (PDFs) were calculated with the R software (version 3.2.5) from measurements observed for the living cells. Figures 6a-6c and 7a-7c display the PDFs of σ_{FSC}, σ_{SSC} and D for living cells of THAL and CHLAM. The median value of (σ_{FSC}), (σ_{SSC}) and D, named $\tilde{\sigma}_{FSC}$, $\tilde{\sigma}_{SSC}$ and $\tilde{D}$, were calculated from the

Optics EXPRESS

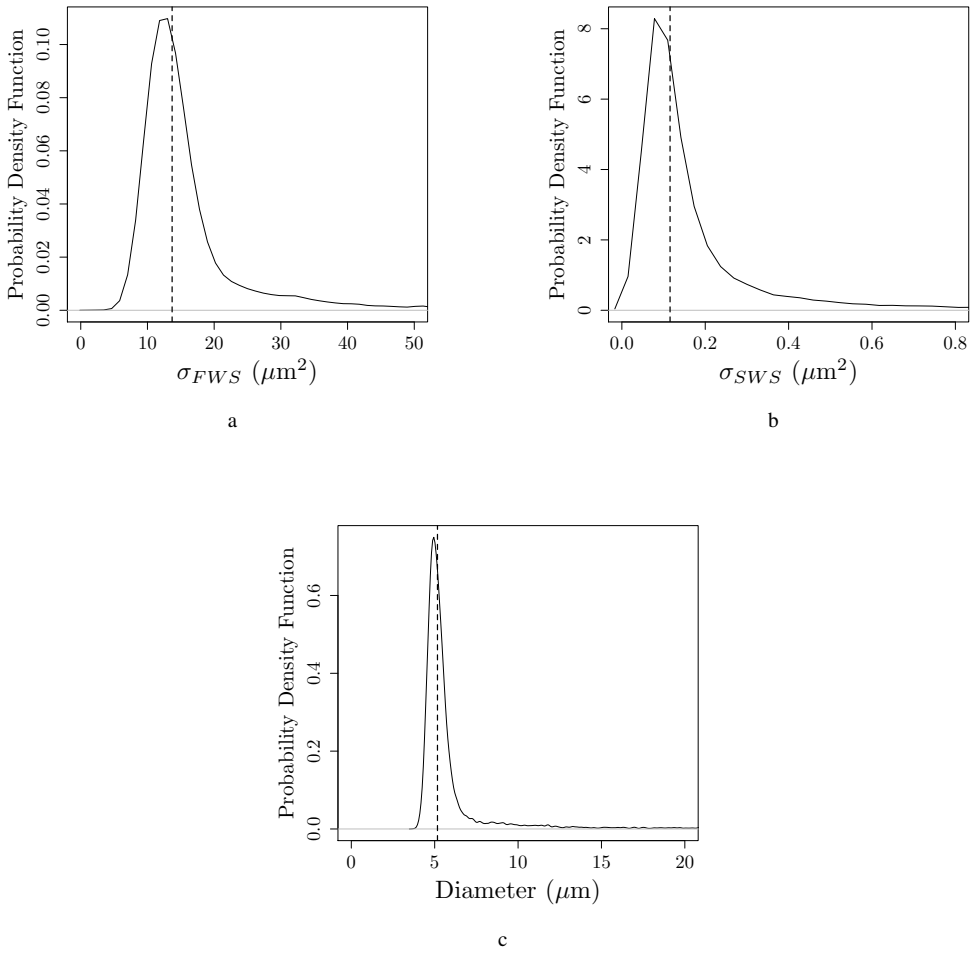

Fig. 6. Probability density function of (a) forward (b) sideward cross sections (μm^2) and (c) diameter of *Thalassiosira pseudonana* the fourth day experiment (21667 values). The dotted lines correspond to the median values.

PDFs. Results presented on the figures 6a-6c and 7a-7c correspond to measurements realized four days after the beginning of the experiment, during the exponential phase.

For CHLAM and THAL, about one per cent of the data corresponded to particles with a diameter between 40 and 100 μm. These values were much higher than diameters measured from SEM and also with diameters referenced in literature for the two species ([14, 27, 28]) but pulse shape flow cytometry records as well aggregates composed of several individual cells. We wanted to exclude any outliers, a cut-off value was applied at the last percentile (q = 0.99) to obtain a population representative of each species. Then, the median value was calculated for the forward ($\tilde{\sigma}_{FSC}$), sideward ($\tilde{\sigma}_{SSC}$) and cell diameter ($\tilde{D}$). The median value was preferred to the mean value as the PDFs of cross sections do not follow a Gaussian distribution. The median values are close to the PDF maximum, whereas mean values are much higher. For cross sections, median values were similar between the two species: $\tilde{\sigma}_{FSC}$ is 13.75 and 13.5 μm^2 and $\tilde{\sigma}_{SSC}$

Optics EXPRESS

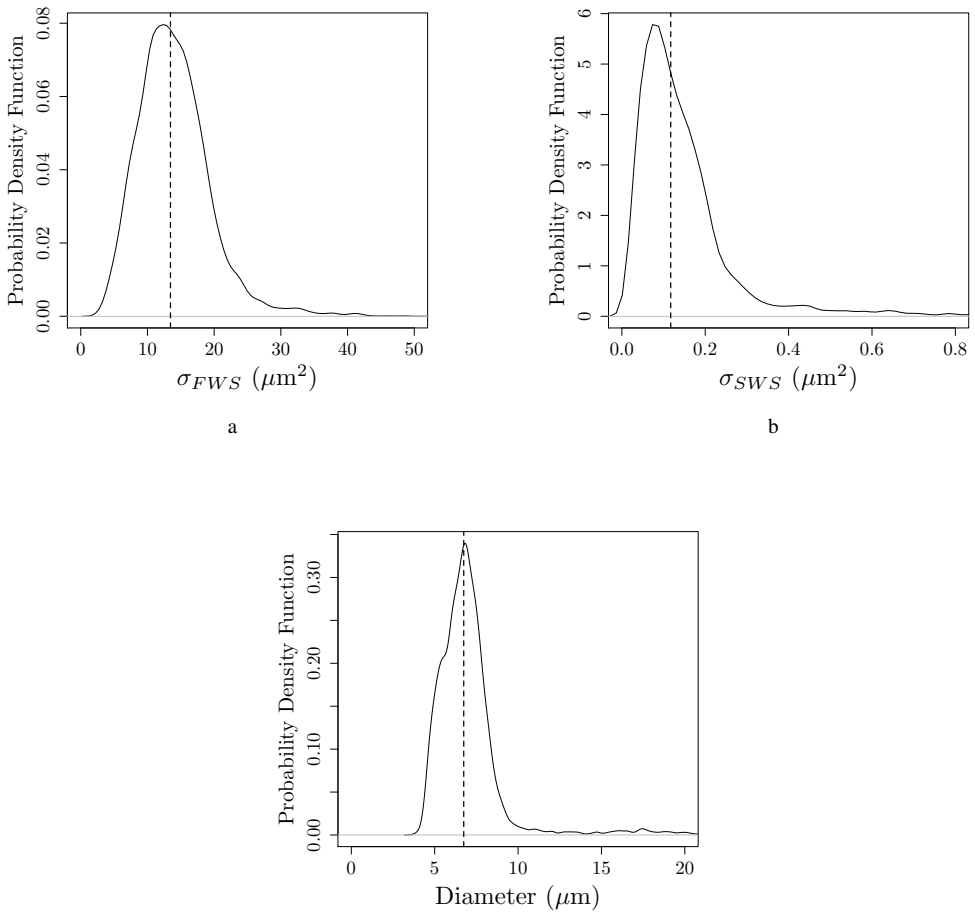

Fig. 7. Probability density function of (a) forward (b) sideward cross sections (μm^2) and (c) diameter of *Chlamydomonas concordia* the fourth day experiment (4638 values). The dotted lines correspond to the median values.

is 0.118 and 0.117 μm^2 for CHLAM and THAL, respectively. However, in terms of scattering efficiency, differences were observed between CHLAM and THAL (see section 3.6). Concerning the diameter, the median was of 6.76 μm for CHLAM and 5.17 μm for THAL with a minimum and maximum values of 3.8 and 21.6 μm, and 3.7 and 39 μm, respectively.

3.4. *Comparison of the measured and theoretical values of forward and sideward cross sections*

The first step consists in checking that the Cytosense estimates of σ_{FSC} and σ_{SSC} for the cultures, were consistent with values as predicted by theory. The comparison exercise was based on radiative transfer simulations because for phytoplankton cultures, *in situ* measurements of forward or sideward cross sections, particle by particle, are not available in literature. As explained previously, the T-Matrix code for oblate and prolate cylinders is limited to $\rho < 10$,

Optics EXPRESS

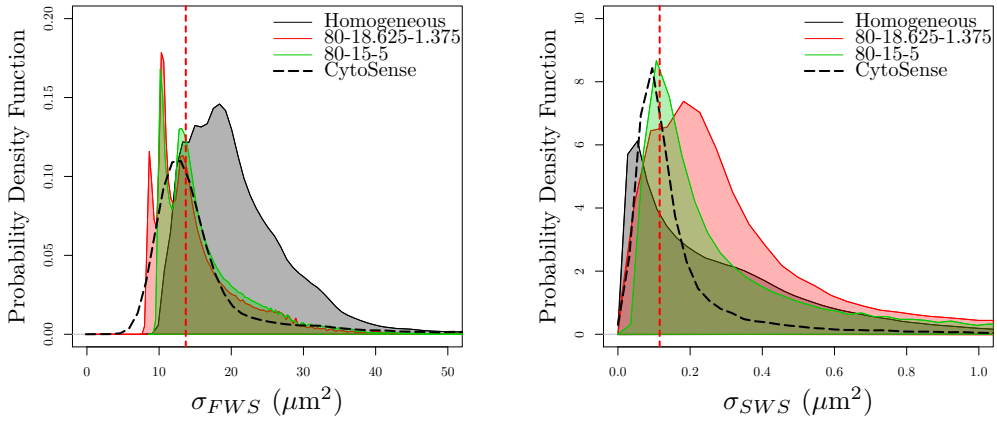

Fig. 8. Probability density function of (a) forward and (b) sideward cross sections (μm^2) simulated according to different models. The models plotted are: homogeneous sphere (gray), 80%$_{cyto}$-18.625%$_{chl}$-1.375%$_{Si}$ (red) and 80%$_{cyto}$-15%$_{chl}$-5%$_{Si}$ (green). The dotted lines are PDF derived from the Cytosense measurements of THAL, equivalent at the Fig. 6. The red dotted vertical lines correspond to the median of Cytosense measurements.

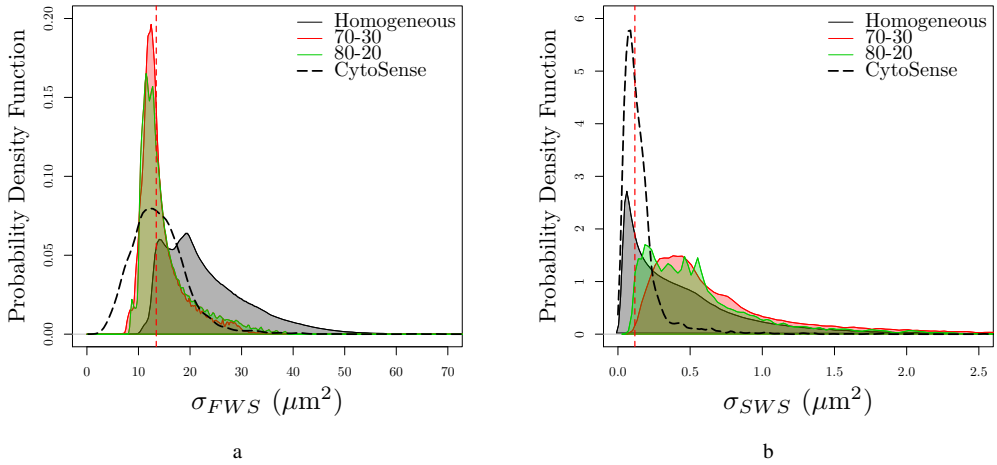

Fig. 9. Probability density function of (a) forward and (b) sideward cross sections (μm^2) simulated according to different models. The plotted models are: homogeneous sphere (gray), 70%$_{cyto}$-30%$_{chl}$ (red) and 80%$_{cyto}$-20%$_{chl}$ (green). The dotted lines are PDF derived from the Cytosense measurements of CHLAM, equivalent at the Fig. 7. The red dotted vertical lines correspond to the median of Cytosense measurements.

which correspond to D <8 μm. This code is not used for the comparison exercise because it does not allow to encompass entirely the particle size distribution (PSD) of the sample. For this

Optics EXPRESS

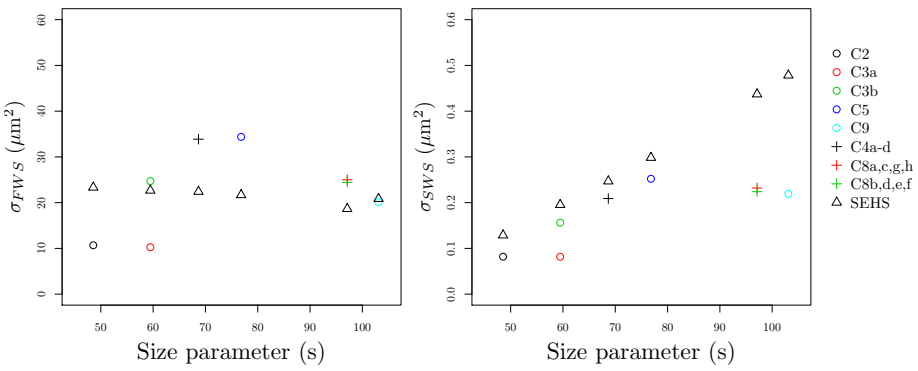

(a) (b)

Fig. 10. (a) The forward and (b) sideward cross sections for aggregates with a symmetric plane (empty circle) without a symmetric plane (cross) and surface equivalent homogeneous sphere (SEHS; empty triangle) as a function of the size parameter (s).

comparison, we used only computations of ScattnLay code (DTB2). For THAL, the Cytosense measurements were compared with computations of three-layer spheres (80%$_{cyto}$-18.625%$_{chl}$-1.375%$_{Si}$ and 80%$_{cyto}$-15%$_{chl}$-5%$_{Si}$) standing for particles with a silica frustule (Fig. 8). For CHLAM, they were compared with computations of two-layered spheres only (Fig. 9). As the particle size impacts the cross section, simulations were multiplied by the particle size distribution measured on the sample by the Cytosense (Figs. 6c and 7c). Thus, measured and simulated cross sections were directly compared. Study cases corresponding to homogeneous spheres were also considered as reference cases. For clarity, simulated forward and sideward cross sections are only provided in Fig. 8 for three sphere models. Some σ_{SSC} values for homogeneous spheres are in the same order of magnitude than those observed for coated spheres. It corresponds to study cases for which homogeneous spheres have a higher equivalent real refractive index (m_{rm}). If we consider the same m_{rm} for homogeneous and coated spheres, homogeneous spheres have always a weaker σ_{SSC} than heterogeneous spheres, and consequently have a higher σ_{FSC}. For instance, considering a 5 μm sphere and $m_m = 1.05 + i0.01$, $\tilde{\sigma}_{SSC}$ increases from 0.11 μm^2 using the homogeneous model to 0.20 μm^2 using the 80%$_{cyto}$-18.625%$_{chl}$-1.375%$_{Si}$ model. For heterogeneous spheres, the variation of the refractive index inside the cell influences internal and external electromagnetic fields ([8,52]). It implies more multiple internal reflections that increase the proportion of side or backscattering light and so decrease the proportion of forward scattering light. For σ_{SSC}, the position and the sharpness of the PFD maximum vary with the considered model. It highlights that the sideward scattering as the backscattering, is more influenced by the cell structure than the forward scattering ([5, 23, 34, 53]). These results obtained from a very large and complete database are conform with previous studies ([5,54]). For CHLAM, lowest values of σ_{FSC} and σ_{SSC} were not featured by the simulations; they represent 9% and 16% of CHLAM data, respectively. It may evidence a slight underestimation of the Cytosense estimates as pointed out in Duforêt-Gaurier *et al.*, 2015. In some cases, the aggregate formation could also induce some low σ_{FSC} values. We compared σ_{FSC} and σ_{SSC} for sphere aggregates with σ_{FSC} and σ_{FSC} and σ_{SSC} for their respective surface equivalent homogeneous spheres. Aggregates C_2, C_{3a} and C_9 displays lower σ_{FSC}, whereas aggregates C_{3b}, C_4, C_5 and C_8 display higher σ_{FSC} (Fig. 10). For the sideward scattering, the σ_{SSC} are always lower for aggregates than for surface equivalent homogeneous spheres. Overall, the aggregate formation tends to decrease the

scattering. For aggregates with a symmetric plane, the σ_{SSC} and σ_{FSC} decrease in average of 37% and 10% respectively. As previously explained, the cell heterogeneity tends to decrease the forward scattering. So, if we combine the impact of cell heterogeneity and cell aggregation, we suppose that the forward scattering will be smaller. Unfortunately, this hypothesis cannot be tested, as to our knowledge, no code, in free access, simulates the optical properties of oriented aggregates formed by heterogeneous spheres.

3.5. The backscattering cross section

For each particle, the sideward cross section is converted into the backscattering cross section (σ_{b_b}) from a theoretical relationship as in Duforêt-Gaurier *et al*., 2015 :

$$\sigma_{b_b}(488) = 10^{-0.6} \times \sigma_{SSC}(488)^{1.09} \quad (R^2 = 0.9). \tag{11}$$

The Eq. (11) was established from the Duforêt-Gaurier *et al*., 2015's theoretical database including 450,000 simulations from the ScattnLay code. In this study, 140,000 study cases were added to the existing database to consider three-layered sphere with ($80\%_{cyto}$-$15\%_{chl}$-$5\%_{Si}$) and silica beads with a refractive index of 1.09 (only silica beads with a refractive index of 1.07 were previously considered in the Duforêt-Gaurier *et al*., 2015's database). This explains why the coefficients of Eq. (11) are slightly different from the coefficients of the Duforêt-Gaurier *et al*., 2015's relationship. In the framework of the microcosm experiment, two specific theoretical relationships were developed to account for the cell structures of CHLAM and THAL, more precisely. The theoretical relationship P2 was established from computations of the $80\%_{cyto}$-$20\%_{chl}$ sphere model, whereas P3 was calculated only from computations of the $80\%_{cyto}$-$18.625\%_{chl}$-$1.375\%_{Si}$ sphere model. Note that P3, stands for particles with a silica wall as THAL. The P1 relationship is calculated from computations of homogeneous spheres only. Estimates derived from P1 will be compared with estimates derived from P2 to highlight the impact of the heterogeneity. P1, P2 and P3 are:

$$(P1) \quad \sigma_{b_b}(488) = 10^{-0.77} \times \sigma_{SSC}(488)^{1.16} \quad (R^2 = 0.96) \tag{12}$$

$$(P2) \quad \sigma_{b_b}(488) = 10^{-0.56} \times \sigma_{SSC}(488)^{1.1} \quad (R^2 = 0.98) \tag{13}$$

$$(P3) \quad \sigma_{b_b}(488) = 10^{-0.59} \times \sigma_{SSC}(488)^{1.04} \quad (R^2 = 0.82). \tag{14}$$

For each daily Cytosense analyze and each batch, the median ($\tilde{\sigma}_{b_b}$) was calculated from the σ_{b_b} distribution of living phytoplankton cells. The values for the two batches of each species were similar. Thus, the mean $\tilde{\sigma}_{b_b}$ per species was calculated with its associated standard deviation over the time period of the exponential growth phase (named $< \tilde{\sigma}_{b_b}^{expo} >$) (Table 3). We do not present the mean $< \tilde{\sigma}_{b_b} >$ calculated over the other growth phases as referenced values in the literature concerned only the exponential phase. Concerning THAL, using the parametrization P3, which stands for particles with a silica wall, the $< \tilde{\sigma}_{b_b}^{expo} >$ is higher of about 11% than the value obtained using the global parametrization. Similarly, for CHLAM, the $< \tilde{\sigma}_{b_b}^{expo} >$ is higher of about 6% using P2 than the mean value obtained using the global parametrization. For THAL and CHLAM, using the parametrization P1, $< \tilde{\sigma}_{b_b}^{expo} >$ is about 60% lower than the values obtained using the global parametrization. The latter highlights that the backscattering signal is underestimated when the phytoplankton cells are considered as a homogeneous spheres.

In this section, the $< \tilde{\sigma}_{b_b} >$ estimates will be compared with references values found in the literature. Unfortunately, as we did not find some referenced measurements of backscattering cross sections for CHLAM, the comparison exercise was only realized for THAL. The σ_{b_b} of THAL has already been studied by Stramski *et al*., 1997 ([14]), Vaillancourt *et al*., 2004

Optics EXPRESS

Table 3. The mean values of the backscattering cross sections (μm^2) for THAL and CHLAM during the exponential phase according to different parametrizations. Note that P3 is applied only for THAL as CHLAM are naked cells.

THAL

Parametrizations	$< \tilde{\sigma}_{b_b}^{expo} > (\mu m^2)$
Global	0.035±0.013
homogeneous spheres (P1)	0.021±0.008
80%-20% (P2)	0.037±0.014
80%-18.625%-1.375% (P3)	0.039±0.013

CHLAM

Parametrizations	$< \tilde{\sigma}_{b_b}^{expo} > (\mu m^2)$
Global	0.036±0.01
homogeneous spheres (P1)	0.021 ± 6.10^{-3}
80%-20% (P2)	0.038±0.011

([27]) and Whitmire *et al*., 2010 ([28]). Stramski *et al*., 1997 derived the refractive index of different phytoplankton cultures from measurements of the PSD, $a(\lambda)$ and $c(\lambda)$. Then, the refractive index and the PSD are used as inputs to simulate the scattering phase function using Mie theory from which the backscattering cross section is derived. For THAL, Stramski *et al*., 1997 found low values around 0.008 μm^2 at 488 nm. This large difference with our results was expected because the backscattering estimates from Stramski *et al*., 1997 were obtained from the Mie theory. As discussed previously, considering homogeneous spheres underestimates greatly σ_{b_b}. We note that the mean value obtained from P1, which considers only computations for homogeneous spheres, is higher than value obtained by Stramski *et al*., 1997. Indeed, Stramski *et al*., 1997 used a real refractive index of about 1.045 while P1 is obtained from radiative transfer simulations considering real refractive indices between 1.03 and 1.09. The imaginary refractive index is of about 0.007 for Stramski *et al*., 1997 and between 0.001 and 0.015 for P1. Vaillancourt *et al*., 2004 used a HOBI Labs Hydroscat-6 (HS6) or an ECO-VSF (WETLabs) to measure b_b during the exponential phase of batch cultures. They achieved the phytoplankton abundance by microscopic counts or flow cytometry. A digital image analysis of cells under epifluorescence microscopy was realized to estimate the biovolume and derive the equivalent size diameter. Vaillancourt *et al*., 2004 found values around 0.041 and 0.054 μm^2 at 470 and 510 nm, respectively. They measured the abundance of BAC for all the cultures. Contaminated cultures were removed from their study. During the exponential phase of our experiment, we found, especially with the P3 relationship, values similar to Vaillancourt *et al*., 2004's ones. Whitmire *et al*., 2010 carried out measurements of b_b with an HOBI Labs Hydroscat-6 (HS6) and obtained the cell concentration, N, from a Coulter counter. During the exponential growth stage, Whitmire *et al*., 2010 referenced, at 442 nm, σ_{b_b} values of 0.149 μm^2 and 1.95 μm^2 for THAL suspensions, coming from two different culture collections. The authors explained such differences by the impact of the cell size on the backscattering signal. Indeed, the mean equivalent size diameter, derived from fitting a Gaussian function to the Coulter counter frequency distribution, was very different between the two THAL suspensions (4.2 μm and 13.93 μm).

Optics EXPRESS

Table 4. The mean values of the efficiency factor for THAL and CHLAM during the exponential phase according to different parametrizations. Note that P3 is applied only for THAL as CHLAM are naked cells.

THAL

Parametrizations	$< \tilde{Q}_{b_b}^{expo} >$
Global	$1.06.10^{-3} \pm 2.6.10^{-4}$
homogeneous spheres (P1)	$6.3.10^{-4} \pm 1.5.10^{-4}$
80%-20% (P2)	$1.14.10^{-3} \pm 2.8.10^{-4}$
80%-18.625%-1.375% (P3)	$1.2.10^{-3} \pm 2.9.10^{-4}$

CHLAM

Parametrizations	$< \tilde{Q}_{b_b}^{expo} >$
Global	$7.53.10^{-4} \pm 1.3.10^{-4}$
homogeneous spheres (P1)	$4.5.10^{-4} \pm 7.9.10^{-5}$
80%-20% (P2)	$8.1.10^{-4} \pm 1.4.10^{-4}$

At the same growth stage, we found lower values. Differences with Whitmire *et al*., 2010 may be explained by a possible underestimation of our estimates due to the empirical relationship. Indeed, Duforêt-Gaurier *et al*., 2015 noticed that in some cases the empirical relationship can underestimate the backscattering cross section. Nevertheless, Whitmire *et al*., 2010 realized bulk measurements instead of single cell ones. It implies that non algal particles, as bacteria can increase $\tilde{\sigma}_{b_b}$. Although, Whitmire *et al*., 2010 assume a low bacteria contamination, they did not realize measurements of bacteria abundance and so did not quantify precisely their possible influence on their estimates. Differences with Whitmire *et al*., 2010 and Vaillancourt *et al*., 2004 could be due to the difference of wavelength. It is rather difficult to quantify the impact of the wavelength. Actually, the backscattering coefficient, and consequently the cross section, do not follow a linear curve with the wavelength (Fig. 3 of [28]).

For applications in natural waters, a specific relationship for diatoms could be used. It will required to re-calculate P3 from a larger database including three-layered sphere computations accounting for different thicknesses for the silica wall. Nevertheless, the use of the global parameterization is more straightforward as it required only to identify living cells. The use of a specific relationship would require a more detailed analysis of the cytograms to isolate carefully diatom cells.

3.6. The backscattering efficiency factor

The backscattering efficiency factor is derived from σ_{b_b} and D estimated from the Cytosense ($\tilde{Q}_{b_b}$) (Eq. (9)) and compared with referenced values. The mean values of $\tilde{Q}_{b_b}$ were calculated for CHLAM and THAL, only for the exponential phase (Table 4). Estimates obtained from P1, P2 and P3 were compared as previously done for σ_{b_b}. For CHLAM, the $< \tilde{Q}_{b_b}^{expo} >$ is higher of about 8% using P2 than the mean value obtained using the global parametrization. Similarly, for THAL, using the parametrization P3, the $< \tilde{Q}_{b_b}^{expo} >$ is higher of about 13% than the value obtained using the global parametrization. For THAL, during the exponential phase, Whitmire *et al*., 2010 referenced Q_{b_b} values of $1.1.10^{-2}$ and $1.3.10^{-2}$ at 442 nm, while Vaillancourt *et al*., 2004 reported values of $4.3.10^{-3}$ and $3.3.10^{-3}$ (at 470 and 510 nm

Optics EXPRESS

respectively). Our estimates, especially using the parametrization P3, are close to one of the two values measured by Vaillancourt *et al*., 2004. Differences can be explained as previously

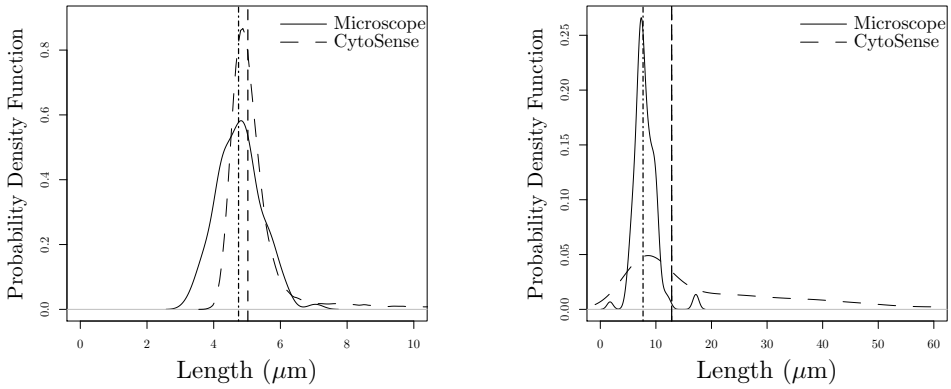

Fig. 11. Length of THAL from the optical microscope (solid lines) and from the Cytosense (long dashed lines) for a) the 4^{th} and b) the 13^{th} day of the experiment. The vertical dashed lines represent the medians values.

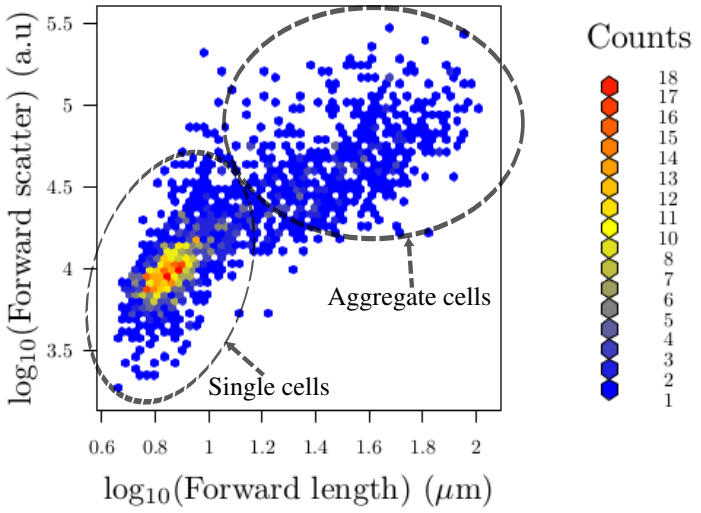

Fig. 12. Cytogram of the total forward (a.u) as a function of the forward length (μm) as estimated from the Cytoclus software. The two dashed black ellipses encompass approximatively the aggregate and single cells. Color bar represent the cells density.

(difference of wavelength, underestimation of the Cytosense estimates, ...) but differences may be also explained by inaccuracies on the cell diameter as derived from the Cytosense. The Cytosense derives the longer axis of the particle (L) on the basis of the length of the recorded signal at half maximum. Some inaccuracies can occur on the Cytosense measurement of L. For THAL, the

Optics EXPRESS

PDF of L observed from optical microscopy (L_{Mic} (μm)) is compared with the PDF derived from the Cytosense (L_{Cyt} (μm)). Results are presented, on Fig. 11, for the 4^{th} and the 13^{th} day of the experiment. The mean EPS was of 0.9 (day 4) and 0.6 (day 13). For the 4^{th} day, the median values of the PDFs obtained were very close: $\tilde{L}_{Mic}$ = 4.75 μm and $\tilde{L}_{Cyt}$ = 5 μm. Concerning the 13^{th}, differences between $\tilde{L}_{Mic}$ and $\tilde{L}_{Cyt}$ were large ($\tilde{L}_{Mic}$ = 7.7 μm and $\tilde{L}_{Cyt}$ = 12.8 μm) but the PDF modes were closer (${L_{Mic}}^{mod}$ = 7.4 μm and ${L_{Cyt}}^{mod}$ = 8.7 μm). First, the differences may be caused by an under-sampling during the optical microscopy analysis. Indeed, the $\tilde{L}_{Mic}$ was calculated from 107 observations, while the $\tilde{L}_{Cyt}$ was calculated from 997 observations. Second, flow cytometry images showed that THAL cells formed aggregates at the end of the experiment. Figure 12 displays the density plot of the forward scatter vs. the forward length for THAL on the 13^{th} day. We observe a high concentration of points (63%) for length between 4 and 13 μm. These points correspond to the single cells and highlight the PDF mode. As the microscope only measures the size of single cells, it explains why the PDF mode of the microscope and the cytometer measurements are close. The aggregated cells, having a higher length and being less concentrate, impact especially the median value. If we considered only the single cells, the PSDs estimated from optical microscopy and from cytometry become very close : $\tilde{L}_{Mic}$ = 7.7 μm and $\tilde{L}_{Cyt}$ = 8.2 μm. We note that, on the 13^{th} day, the aggregated cells represented about 37% of the total number of cells, while they represented 5% on the 4^{th} day. Similarly, Engel in 2000 ([55]) observed in the western Baltic Sea an enhance of the apparent coagulation efficiencies, and so aggregation, at the decline of a diatom bloom. This improvement was associated with an increase of the transparent exopolymer particles (TEP). TEP are sticky and their abundance may enhance the probability of particle collisions. Thus, they could control coagulation efficiencies and cause the formation of aggregates at the end of the bloom ([55, 56]). An other sources of inaccuracies on D_e is due to the eccentricity. For particles with a high eccentricity, D_e is significantly different from the longer axis. It results that considering $D_e = \tilde{L}_{Cyt}$ introduce inaccuracies on the scattering efficiencies (Eq. (9)). Figure 13 compares for the 4^{th} and 13^{th} day of the experiment, L_{Cyt} with D_e calculated from optical

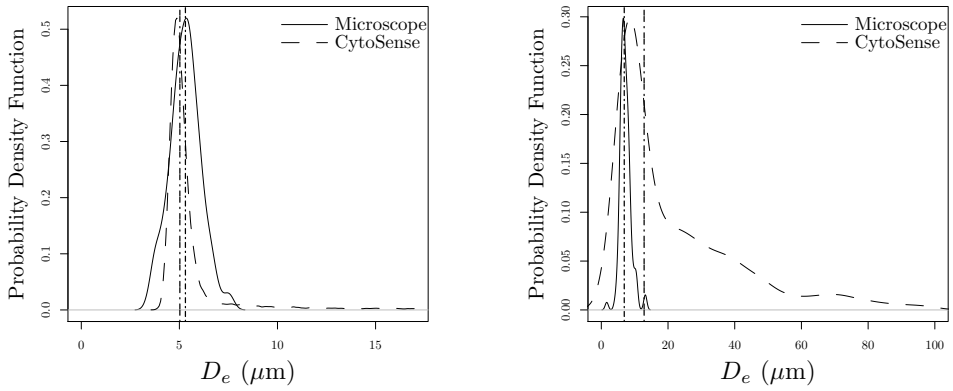

Fig. 13. Equivalent diameter of THAL from the optical microscope (solid lines) and longer axis from the Cytosense (long dashed lines) for a) the 4^{th} and b) the 13^{th} day of the experiment. The vertical dashed lines represent the medians values.

Optics EXPRESS

microscopy observation:

$$D_e = \sqrt{\frac{{l_{Mic}}^2}{2} + (l_{Mic} \times L_{Mic})}, \quad (15)$$

with l_{Mic} the smaller axis of the particle. Figure 13a highlights that, for an EPS of 0.9, L_{Cyt} and D_e are very close with $\tilde{L}_{Cyt}$ and $\tilde{D}_e$ of 5 μm and 5.3 μm, respectively. As expected, the differences between L_{Cyt} and D_e increase for a higher eccentricity. For an EPS of 0.6: $\tilde{D}_e$ is of 6.9 μm and $\tilde{L}_{Cyt}$ is of 12.8 μm (Fig. 13b). The modes of the PDF are also different: ${L_{Cyt}}^{mod}$ = 8.7 μm and ${D_e}^{mod}$ = 6.6 μm. We note that, for the 4^{th} (EPS = 0.9) and the 13^{th} (EPS = 0.6) days, use $\tilde{L}_{Cyt}$ instead of D_e induce an absolute error of around 20 % on Q_{b_b}.

4. Discussion and conclusion

The methodology of Duforêt-Gaurier *et al*., 2015 was applied for the first time on phytoplankton cultures (*Thalassiosira pseudonna* et *Chlamydomonas concordia*). For the first time, cytometric measurements of the scattering of phytoplankton cells permitted to estimate their scattering cross sections and efficiencies.

Most of the Cytosense estimates of the forward and sideward cross sections for the cultures are in agreement with values predicted by the theory. For CHLAM, only the lowest values of σ_{FSC} and σ_{SSC} are not consistent with the simulations but they represent only 9% and 16 % of the total forward and sideward measurements, respectively. Discrepancies may be due to the method itself. As pointed out by Duforêt-Gaurier *et al*., 2015, a source of errors may result in inaccuracies in the modeling of the Cytosense weighting functions during the calibration process. The authors noticed a slight underestimation of the Cytosense estimates when they compared their Cytosense estimates with ECO-BB9 measurements on bead suspensions. Discrepancies may be due to the codes used in this comparison exercise. The codes simulate the scattering and absorbing processes of an incident plane wave radiation, whereas the Cytosense laser beam is a Gaussian wave. Duforêt-Gaurier *et al*., 2015 (as previously Ackleson and Spinrad, 1988 ([57])) have already discussed this issue. They noticed that the Mie predictions were in agreement with their NIST traceable measurements. Moreover, they observed that differences between predicted and observed cross sections did not increase with particle size. Duforêt-Gaurier *et al*., 2015 concluded that for particle size less than 80 μm, errors due to the plane wave assumption were probably small because the horizontal dimension of the laser beam (300 μm) was large relative to the size of the particles. To analyze more fully this issue, we could use the algorithm of Mackowski *et al*., 2011 ([58]). This code simulates absorption and scattering of an incident Gaussian wave by an homogeneous sphere and/or a sphere cluster. However, the code inputs are not trial because the incident Gaussian wave have to be perfectly characterized. As the CytoSense laser undergoes a beam shaping, its optical characteristics (as the beam width and the focal point) are modified through the optical system. For this reason, it is extremely complex and so challenging to accurately define the optical characteristics of the laser beam. Moreover, to our knowledge, no free access operational code exits to simulate the scattering of an incident Gaussian wave by an heterogeneous particle. Thus, if we want to take into account the Gaussian laser beam, we are limited to homogeneous spheres or homogeneous sphere clusters.

The $< \tilde{\sigma}_{b_b}^{expo} >$ and $< \tilde{Q}_{b_b}^{expo} >$ values of THAL, fall within the range of *in situ* measurements realized by Vaillancourt *et al*., 2004 but were smaller than *in situ* measurements of Whitmire *et al*., 2010. As σ_{b_b} is derived from σ_{SSC}, calibration inaccuracies on σ_{SSC} directly impact σ_{b_b} and constitute a first source of errors. Moreover, the scattering of data around the mean relationship (Eq. (11)) introduces inaccuracies on σ_{b_b} estimates. In future studies, a specific relationship by phytoplankton functional types could be used to reduce the variability around the mean relationship. In a first time, the idea is to develop, for example, three relationships: one for the calcifiers, one for the silicifiers and one for the other types. Calcifiers and silicifiers presents

Optics EXPRESS

well-defined structural characteristics with their respective calcite and silica wall, which can be well-identified to be modeled by the radiative transfer codes ([2, 3, 7, 52, 59]). Discrepancies on σ_{b_b} with referenced values may also come from the difference of the type of measure: bulk measurements for backscattering sensors against and single cells measurements for the Cytosense. Duforêt-Gaurier *et al.*, 2015 showed relative differences between 20% and 25% between simulations of monodispersed and polydispersed beads. Estimates of the scattering efficiencies $< \tilde{Q}_{b_b} >$ depend on the size accuracy as $< \tilde{Q}_{b_b} >$ is defined as the ratio of σ_{b_b} to the geometrical cross section (Eq. (9)). Discrepancies were observed for calibration beads between the length derived from the Cytosense and the length as indicated by the manufacturer, more particularly for bead diameters less than < 10 μm ([60]). Different studies are carried out by many research teams to improve the length estimates. Recently, Dugenne *et al.*, 2014 ([61]), who worked on larger cells, showed a correlation between the sideward signal and the cell biovolume thanks to the images collected with the "image in flow" device and taking into account the pulse shape of SSC per cell. Unfortunately, in the framework of this study, THAL and CHLAM cells were too small to apply the improvements proposed by Dugenne et al., 2014. The method of Duforêt-Gaurier et al., 2015 seems promising and in combination with adapted radiative transfer computations, will strongly enhance the impact of phytoplankton cells on the sideward and backscattering signal.

Acknowledgments

The authors gratefully acknowledge the support from the French Space Agency (CNES) through the TROPHY project (CNES/TOSCA program) and the PHYTOCOT project (CNES/TOSCA program). William Moutier is supported by the French Ministry of Higher Education through a PhD grant. The authors thank Dr. Annick Bricaud (Laboratoire d'Océanologie de Villefranche, France), Dr. Natacha Guiselin and Anne-Hélène Rêve (Laboratoire d'Océanologie et de Géoscience, France) for their precious advice. Thanks to Laurent Brutier (LOG/ULCO), Arnaud Cauvin and Michel Laréal for their technical help.